Horizon-absorption effects in coalescing black-hole binaries: An effective-one-body study of the nonspinning case

Horizon-absorption effects in coalescing black-hole binaries: An effective-one-body study of the non-spinning case.

Sebastiano Bernuzzi,[1] Alessandro Nagar,[2] and Anıl Zenginoğlu[3]

[1] *Theoretical Physics Institute, University of Jena, 07743 Jena, Germany*
[2] *Institut des Hautes Etudes Scientifiques, 91440 Bures-sur-Yvette, France*
[3] *Theoretical Astrophysics, California Institute of Technology, Pasadena, California, USA*

We study the horizon absorption of gravitational waves in coalescing, circularized, nonspinning black hole binaries. The horizon absorbed fluxes of a binary with a large mass ratio ($q = 1000$) obtained by numerical perturbative simulations are compared with an analytical, effective-one-body (EOB) resummed expression recently proposed. The perturbative method employs an analytical, linear in the mass ratio, effective-one-body (EOB) resummed radiation reaction, and the Regge-Wheeler-Zerilli (RWZ) formalism for wave extraction. Hyperboloidal layers are employed for the numerical solution of the RWZ equations to accurately compute horizon fluxes up to the late plunge phase. The horizon fluxes from perturbative simulations and the EOB-resummed expression agree at the level of a few percent down to the late plunge. An upgrade of the EOB model for nonspinning binaries that includes horizon absorption of angular momentum as an additional term in the resummed radiation reaction is then discussed. The effect of this term on the waveform phasing for binaries with mass ratios spanning 1 to 1000 is investigated. We confirm that for comparable and intermediate-mass-ratio binaries horizon absorbtion is practically negligible for detection with advanced LIGO and the Einstein Telescope (faithfulness ≥ 0.997).

PACS numbers: 04.30.Db, 04.25.Nx, 95.30.Sf, 97.60.Lf

I. INTRODUCTION

The dynamics of the quasi-circular inspiral of coalescing binary black hole (BBH) systems is driven by the loss of mechanical angular momentum through gravitational radiation. The total loss of angular momentum consists of two contributions: the one due to radiation emitted to future null infinity ($\mathcal{F}^{\mathscr{I}}_{\varphi}$), and the one due to radiation absorbed by the black-hole horizons ($\mathcal{F}^{H}_{\varphi}$). Typically the former dominates over the latter, i.e. $\mathcal{F}^{\mathscr{I}}_{\varphi} \gg \mathcal{F}^{H}_{\varphi}$. For example, the leading order contribution to horizon absorption for a nonspinning binary is a 4PN contribution of the form [1–3]

$$\frac{\mathcal{F}^{H}}{\mathcal{F}^{\mathscr{I}}_{N}} = x^4 \left(1 - 4\nu + 2\nu^2\right) \left[1 + c^{H}_{1}(\nu) x + \mathcal{O}(x^2)\right]. \quad (1)$$

Above $x = (M\Omega)^{2/3}$ is the post-Newtonian orbital parameter, Ω is the orbital frequency, $M = M_A + M_B$ is the total mass of the system, with $M_{A,B}$ the masses of the individual black-holes, $\nu = M_A M_B/M^2$ is the symmetric mass ratio, and $\mathcal{F}^{\mathscr{I}}_{N} = \nu^2\, 32/5\, x^{7/2}$ is the Newtonian contribution to the asymptotic flux. The explicit expression of $c^{H}_{1}(\nu)$ follows from the state-of-the-art 1PN-accurate result of Taylor and Poisson [2]. In the presence of spin, a more complicated formula holds [2], with the contribution of absorption entering already as a 2.5PN effect. In practice, horizon absorption is a negligible effect when: (i) the separation between the two objects is large: (ii) the two objects have comparable masses ($\nu \sim 1/4$); (iii) the spins are small.

Leading-order calculations by Alvi [1] (improved to 1PN fractional accuracy by Taylor and Poisson [2]) estimate the effect of horizon flows on the number of gravitational wave (GW) cycles to be no more than 10% of a cycle for comparable-mass ($q = M_B/M_A = 4$) binaries with maximally spinning black holes by the time of merger (see Table IV of Ref. [1]). In the nonspinning case absorption effects seem negligible with accumulated dephasings that are smaller than 1% of a cycle.

The analysis of [1] is, however, inaccurate during the late inspiral and plunge ($1/6 \lesssim x \lesssim 1/3$). In this regime, absorption effects *may be relevant* for GW detection due to relativistic corrections, if the mass ratio or the individual spins are sufficiently high. The potential importance of absorption effects during the late plunge of spinning binaries was also pointed out by Price and Whelan [4] using the close-limit approximation.

To meaningfully ascertain the importance of energy and angular momentum flows in or out of the black holes (depending on the orientation of the spin with respect to angular momemtum) during the late inspiral and plunge, one needs numerical relativity (NR) simulations. The growth rate of the irreducible mass and angular momentum of the black hole horizons in a NR simulation of nearly-extremal spinning black hole binary [5] has been compared to Alvi's analytical prediction. A remarkable numerical agreement between the two was found up to $x \lesssim 0.16$, while significant deviations from numerical data were observed for larger values of x. This result suggests that horizon-absorption effects should be incorporated in the analytical modeling of coalescing black hole binaries.

To bridge the gap between the leading-order estimate of Alvi valid during the early inspiral [1] and the qualitative understanding of Price and Whelan valid during the late plunge [4] one needs an analytic description of the absorbed fluxes that incorporates high-order PN correc-

tions and that is not limited to the slow-velocity, weak-field regime. Focusing on nonspinning binaries, Ref. [3] adapted the resummation procedure of the asymptotic energy flux of Ref. [6] to the energy flux absorbed by the two black holes, so to consistently incorporate it within the effective-one-body (EOB) [7–9] description of the dynamics of black hole binaries. The final outcome of that study is an analytical expression of the absorbed energy flux, written in a specific *factorized and resummed form*, that is well-behaved (contrary to a standard, PN expansion) also in the strong-field-fast-velocity regime (notably, also along the EOB-defined sequence of unstable circular orbits). The input for the resummation procedure is given by state-of-the art PN-expanded results for the horizon flux: the 1PN accurate expressions of Taylor and Poisson [2] (valid for any mass ratio), and the leading-order results of Poisson and Sasaki [10] in the test-mass ($\nu = 0$) limit. In addition, this analytical knowledge was further improved by adding higher-order (effective) PN coefficients extracted from the absorbed fluxes from circular orbits computed numerically in the test-mass limit. Finally, $\nu = 0$ and $\nu \neq 0$ (semi)-analytical results were hybridized to get improved accuracy for any mass ratio.

In this paper we study the effect of horizon-absorption on the phasing of circularized, coalescing black-hole binaries up to merger. We do this by using the EOB description of the binary dynamics and radiation [7–9]. The radiation reaction is improved by an additional term, $\mathcal{F}_\varphi^H$, that takes into account the loss of mechanical angular momentum due to horizon absorption. As a first cut of the problem, we consider here *nonspinning* binaries only, where the effects are weaker than when the BHs are spinning [1].

First of all, we focus on the "large-mass-ratio" limit (e.g., $\nu = 10^{-3}$) and we check the consistency of the ($\nu = 0$) analytical expression of $\mathcal{F}_\varphi^H(x;0)$ proposed in [3] against the absorbed GW flux obtained numerically using a Regge-Wheeler-Zerilli (RWZ) perturbative treatment. This gives further confirmation of the reliability of the resummation and hybridization procedure of the absorbed flux introduced in [3]. Then we perform a comprehensive EOB study to investigate the effect of $\mathcal{F}_\varphi^H(x;\nu)$ on the phasing up to merger with $10^{-3} \leq \nu \leq 1/4$. Note that NR simulations for mass ratios $q = 100$ are currently doable [18–20], though they are challenging, do not yet provide sufficiently long waveforms, and it does not seem practical to cover the parameter space densely with full numerical relativity simulations only. Therefore, the EOB model is of fundamental importance to investigate the so-called intermediate-mass-ratio (IMR) regime [21–25].

The RWZ time-domain perturbative method employed in this work to obtain large-mass-ratio waveforms is described in detail in [26–30]. We solve the RWZ equations for a binary system made of a point-particle on a Schwarzschild background and subject to leading-order, $\mathcal{O}(\nu)$, EOB-resummed analytical radiation reaction. The main technical improvement introduced here is the development of smooth hyperboloidal layers [31] attached to a compact domain of Schwarzschild spacetime in standard coordinates to include both future null infinity, $\mathscr{I}$, and the black-hole horizon, H, in the computation. With this method, the absorbed and radiated fluxes can be computed very accurately. Also, the finite differencing order has been improved to 8th order accurate operators. These technical developments lead to such an efficient code that tail decay rates for the late-time of the gravitational waveform emitted by inspiraling point particles can be computed accurately (this was not possible previously using standard methods).

This paper is organized as follows. In Sec. II we review the results of Ref. [3] that are relevant for this work and we give the explicit expression for $\mathcal{F}_\varphi^H$. In Sec. III we discuss the construction of hyperboloidal layers and their advantages in improving the accuracy of the numerical solution of the RWZ equation. In Appendix A we also demonstrate that the layer technique helps solving a previously difficult problem of obtaining accurate power law tails for inspiraling particles. In Sec. IV we present the RWZ calculation of the absorbed waveforms and flux and the consistency check of $\mathcal{F}_\varphi^H(x\,,0)$. The main results of the paper are collected in Sec. IV C, where we investigate the influence of $\mathcal{F}_\varphi^H$ on the phasing up to merger. Concluding remarks are gathered in Sec. V. We use units with $G = c = 1$.

II. EOB DYNAMICS AND WAVEFORM: INCLUDING HORIZON ABSORPTION

In this Section we review the main elements of the EOB approach and we recall the results of [3] that are needed to compute $\mathcal{F}_H$. The EOB analytical description of the dynamics of a circularized binary essentially relies on two building blocks: the resummed EOB Hamiltonian $H_{\rm EOB}$, which describes conservative effects, and the resummed mechanical angular momentum loss $\mathcal{F}_\varphi$, which describes nonconservative effects due to loss of GW energy (radiation reaction) [2]. The EOB Hamiltonian depends only on the relative position and momenta of the binary system.

[1] Note that the EOB approach can account consistently for (arbitrary) spins [9, 11–14]. Black hole absorption has already been included in EOB-based evolutions of extreme-mass-ratio (EMR) inspirals around a Kerr black hole, though only in its standard Taylor-expanded form [15, 16]. An improved treatment of this problem is currently under development [17].

[2] An additional radiation reaction term, $\mathcal{F}_r$, is present due to linear momentum loss through GWs, but, for circularized binaries, is typically not included because it remains small up to the late plunge.

For nonspinning binaries it has the structure

$$H_{\rm EOB}(r,p_{r_*},p_\varphi) \equiv M\sqrt{1+2\nu(\hat{H}_{\rm eff}-1)}, \qquad (2)$$

where

$$\hat{H}_{\rm eff} \equiv \sqrt{p^2_{r_*}+A(r)\left(1+\frac{p^2_\varphi}{r^2}+z_3\frac{p^4_{r_*}}{r^2}\right)}. \qquad (3)$$

Here $z_3 \equiv 2\nu(4-3\nu)$ and we use rescaled dimensionless variables, namely $r \equiv r_{AB}c^2/(GM)$, where $r_{AB} = |\mathbf{r}_A - \mathbf{r}_B|$, the relative separation between the two bodies, and $p_\varphi \equiv P_\varphi/(GM_AM_B)$, the angular momentum. In Eq. (3), p_{r_*} is the radial momentum canonically conjugate to a EOB-defined tortoise coordinate, r_*, that reduces to the usual tortoise coordinate when $\nu = 0$. The function $A(r)$ is the basic radial potential that, following Ref. [32], depends on two EOB flexibility parameters (a_5, a_6) that take into account effective 4PN and 5PN corrections to the conservative dynamics. For coalescing black-hole binaries, an excellent phasing agreement between NR and EOB waveforms can be reached over banana-like regions in the (a_5, a_6) plane. Following Ref. [32], we fix the EOB parameters as $a_5 = -6.37$ and $a_6 = 50$ which lie within the extended region that yields a good fit with NR data for $q = 1$, 2, and 4. A recent study [33] comparing an (a_5, a_6)-parametrized EOB model with NR simulations for $q = 1$, 2, 3, 4, and 6 (and more accurate than those used in Ref. [32]) pointed out that the "best fitting" region in the (a_5, a_6) plane actually depends on ν (see Fig. 5 in [33]). Since our goal here is to highlight only the effect of $\mathcal{F}^H_\varphi$ on the dynamics, we neglect this further ν-dependence on (a_5, a_6). The analysis of the ν-dependence of (a_5, a_6) in the calibration of the EOB model of Ref. [32], in the presence of black-hole absorption and with better numerical data, is postponed to future work.

The radiation reaction force, $\mathcal{F}_\varphi$, drives the angular momentum loss during evolution. The Hamilton equation for p_φ reads

$$\frac{dp_\varphi}{dt} = \hat{\mathcal{F}}_\varphi, \qquad (4)$$

where $\hat{\mathcal{F}}_\varphi = \mathcal{F}_\varphi/\nu$. The mechanical angular momentum loss is typically written as

$$\hat{\mathcal{F}}_\varphi = -\frac{32}{5}\nu r^4_\omega \Omega^5 \hat{f}(v^2_\varphi;\,\nu). \qquad (5)$$

Here, $\Omega = d\varphi/dt$ is the orbital frequency, with φ the orbital phase, $v_\varphi = r_\omega\Omega$ is the azimuthal velocity, and $r_\omega = r\psi^{1/3}$, where ψ is a ν-dependent correction factor that is necessary to formally preserve Kepler's law during the plunge [34]. The function $\hat{f}(x;\,\nu)$ is the *reduced flux function* that is defined, for a circularized binary, as the ratio between the total energy flux and the $\ell = m = 2$ asymptotic energy flux. In our case the reduced flux function is given by the sum of an asymptotic and a horizon contribution as

$$\hat{f}(x;\,\nu) = \hat{f}^{\mathscr{I}}(x;\,\nu) + \hat{f}^{H}(x;\,\nu), \qquad (6)$$

where each term is given by

$$\hat{f}^{(\mathscr{I},H)}(x;\,\nu) = F^{(\mathscr{I},H)}_{\ell_{\rm max}}/F^{\rm N}_{22}. \qquad (7)$$

Here, $F^{(\mathscr{I},H)}_{\ell_{\rm max}}$ are the total asymptotic ($\mathscr{I}$) and horizon (H) energy fluxes for circular orbits summed up to multipole $\ell = \ell_{\rm max}$, while $F^N_{22} = (32/5)\nu^2x^5$ is the Newtonian quadrupolar (asymptotic) energy flux. In the EOB model one uses suitably factorized expressions for the multipolar fluxes $F^{(\mathscr{I},H)}_{\ell m}$ to resum and improve them with respect to standard PN-expanded expressions in the strong-field, fast-velocity regime ($1/6 \lesssim x \lesssim 1/3$). The resummation of the asymptotic waveform and fluxes was discussed in Ref. [6] and has been used in many works since then. We use it here at the 3^{+2}PN accuracy [3] and we fix $\ell_{\rm max} = 8$.

The horizon flux is written as the sum (up to $\ell_{\rm max} = 8$)

$$F^{H,(\ell_{\rm max})}(x;\,\nu) = \sum_{\ell=2}^{\ell_{\rm max}}\sum_{m=1}^{\ell} F^{(H,\epsilon)}_{\ell m}(x;\,\nu) \qquad (8)$$

where the partial multipolar fluxes have the following factorized structure [3]

$$F^{(H,\epsilon)}_{\ell m}(x;\,\nu) = F^{(H_{\rm LO},\epsilon)}_{\ell m}(x;\,\nu)\left[\hat{S}^{(\epsilon)}_{\rm eff}(x;\nu)\left(\rho^H_{\ell m}(x;\,\nu)\right)^\ell\right]^2. \qquad (9)$$

Here, $\epsilon \equiv \pi(\ell+m) = 0, 1$ is the parity of the considered multipole, $\hat{S}^{(\epsilon)}_{\rm eff}$ is a source factor, with $\hat{S}^{(0)}_{\rm eff} = \hat{H}_{\rm eff}$ or $\hat{S}^{(1)}_{\rm eff} = \sqrt{x}p_\varphi$ according to the parity of the multipole, and the $\rho^H_{\ell m}(x;\,\nu)$ are the residual amplitude corrections to the horizon waveform. Only $\rho^H_{22}(x;\,\nu)$ is known analytically at 1PN accuracy [3]. It reads

$$\rho^{H_{\rm 1PN}}_{22}(x;\,\nu) = 1 + \frac{4-21\nu+27\nu^2-8\nu^3}{4(1-4\nu+2\nu^2)}x + \mathcal{O}(x^2). \qquad (10)$$

To improve our knowledge of the strong-field behavior of the ρ^H_{22} functions, Ref. [3] computed numerically the $\rho^{H_{\rm num}}_{\ell m}$ functions for a test particle moving on (stable and unstable) circular orbits on a Schwarzschild background. For each multipole, it was possible to fit the numerically computed $\rho^{H_{\rm num}}_{\ell m}$ accurately via a suitable rational function of the form

$$\rho^{H_{\rm fit}}_{\ell m}(x) = \frac{1+n^{\ell m}_1 x + n^{\ell m}_2 x^2 + n^{\ell m}_3 x^3 + n^{\ell m}_4 x^4}{1+d^{\ell m}_1 x + d^{\ell m}_2 x^2} \qquad (11)$$

[3] The 3PN-accurate ν-dependent terms are augmented by the 4PN and 5PN accurate $\nu = 0$ corrections for all multipoles.

TABLE I: Coefficients of our hybrid 1^{+3}PN-accurate $\rho^H_{\ell m}(x;\,\nu)$ functions as given by Eq. (13).

ℓ	m	$c_1^{\ell m}$	$c_2^{\ell m}$	$c_3^{\ell m}$	$c_4^{\ell m}$
2	2	$\frac{4-21\nu+27\nu^2-8\nu^3}{4(1-4\nu+2\nu^2)}$	4.78752	26.760136	43.861478
2	1	0.58121	1.01059	7.955729	1.650228
3	3	1.13649	3.84104	45.696716	27.55066
3	2	0.83711	1.39699	23.638062	-1.491898
3	1	1.61064	2.97176	10.045280	15.146875
4	4	1.15290	4.59627	55.268737	13.255971
4	3	0.96063	1.45472	43.480636	-35.225828
4	2	1.43458	2.43232	21.927986	10.419841
4	1	0.90588	1.17477	5.126480	4.022307

where $n_i^{\ell m}$ and $d_i^{\ell m}$ are free fitting parameters [4]. By Taylor-expanding Eq. (11) in powers of x one obtains the following representation of the $\rho^H_{\ell m}$ functions in the $\nu = 0$ limit

$$\rho^H_{\ell m}(x;\,0) = T_N[\rho^{H_{\rm fit}}_{\ell m}(x)], \tag{12}$$

where N indicates the maximum power of the expansion. For the $\ell = m = 2$ mode, Ref. [3] pointed out that setting $N = 4$ (i.e., 4PN accuracy) is sufficient to yield an accurate representation of the $\rho^{H_{\rm num}}_{\ell m}$ up to and below the last-stable-orbit (LSO) at $r = 6$, with relatively small differences around the light-ring (see Fig. 3 of [3]). We have verified that this remains true also for the other multipoles, so that we shall assume 4PN accuracy in Eq. (12) from now on. Following Ref. [3], we *hybridize* the ν-dependent 1PN information of Eq. (10) with the 4PN expansion of Eq. (12). Such hybridization procedure, that is conceptually analogous to what has been done in Ref. [6] for the corresponding asymptotic residual amplitude corrections, is justified in view of the following two results of Ref. [3]: (i) the dependence on ν of the 1PN coefficient in Eq. (10) is mild; (ii) the fit of the numerical data proved to be robust enough so that the coefficients of the PN expansion can be taken as reliable estimates for the actual (yet un-calculated) PN coefficients. In practice we use the following 4PN expression for the $\rho^H_{\ell m}(x;\,\nu)$

$$\rho^H_{\ell m}(x;\,\nu) = 1 + c_1^{\ell m} x + c_2^{\ell m} x^2 + c_3^{\ell m} x^3 + c_4^{\ell m} x^4. \tag{13}$$

The values of the coefficients $c_i^{\ell m}$, $i = 1, \ldots, 4$ are listed in Table I, where in fact only c_1^{22} is given analytically as a function of ν, while the other coefficients are computed from the test-mass $n_i^{\ell m}$ and $d_i^{\ell m}$ coefficients extracted from the fit. We shall use them in the following as an effective representation of the actual test-mass information, although the hope is that it will be soon possible to replace them with terms from a PN calculation.

In Table I we list all PN coefficients up to $\ell = 4$. It seems enough to include only the quadrupolar contributions ρ^H_{21} and ρ^H_{22} in $\hat{f}^H(x;\,\nu)$, since, as we show in Sec. IV below, the effect of multipoles with $\ell \geq 3$ on the horizon-absorbed angular-momentum flux is practically negligible already in small-mass-ratio coalescence events. [Note that the ν-dependence of the leading-order prefactor to the multipolar horizon flux, $F^{H_{\rm LO}}_{\ell m}$ is fully known only for the quadrupole modes [2]].

Using Eqs. (6), (9) and (13) one defines an EOB dynamics that takes into account horizon absorption. From this dynamics one then computes the (asymptotic) EOB multipolar waveform that has the well known factorized structure

$$h_{\ell m} = h^{(N,\epsilon)}_{\ell m}\, \hat{S}^{(\epsilon)}_{\rm eff}\, \hat{h}^{\rm tail}_{\ell m} (\rho_{\ell m})^\ell \hat{h}^{\rm NQC}_{\ell m}, \tag{14}$$

where $h^{(N,\epsilon)}_{\ell m}$ is the Newtonian waveform, $\hat{h}^{\rm tail} \equiv T_{\ell m} e^{i\delta_{\ell m}}$ is the tail factor as defined in Ref. [6], $\rho_{\ell m}$ is the resummed modulus correction and $\hat{h}^{\rm NQC}_{\ell m}$ is a next-to-quasi-circular correction. For each multipole (ℓ, m) these NQC corrections depend on 4 parameters, $a_i^{\ell m}$, $i = 1, \ldots, 4$ (two for amplitude corrections and two for a phase correction) that have to be determined with an iterative procedure to match the EOB waveform to the NR waveform around merger. The NQC correction to the amplitude depending on $(a_1^{\ell m}, a_2^{\ell m})$ is the same as in Refs. [29, 32]; the NQC correction to the phase depending on $(a_3^{\ell m}, a_4^{\ell m})$ is implemented as per Eq. (22) of Ref. [33], that proved more robust than the analogous expression used in Eq. (12) of [29] to complete the EOB waveform in the extreme mass-ratio limit. The $a_i^{\ell m}$ parameters are determined as in [29] by imposing that the slope of the EOB waveform amplitude and frequency agree with the NR ones at the peak of the EOB orbital frequency Ω. Note that, consistently with the findings of [29] and differently from previous work [32, 33], we *do not* impose that the peak of $|h_{22}|$ occurs at the same time as the peak of Ω. On the contrary, we allow $|h_{22}|$ to have a nonzero slope there that coincides with the slope of the NR waveform modulus $|h^{\rm NR}_{22}|$ at a NR time that occurs slightly after the time corresponding to $\max|h_{22}|$. This NR-data extraction point is suitably chosen consistently with the test-mass results [35]. To obtain the coefficients $a_i^{\ell m}$ for any value of ν, we fit with cubic polynomials in ν the NR points extracted from both the waveforms computed for us by D. Pollney and C. Reisswig using the Llama code [35–37], for mass ratios $q = 1, 2, 3, 4$, and the perturbative data of [29, 30]. As a last step we match to the EOB inspiral-plus-plunge waveform, Eq. (14), a superposition of Kerr black-hole quasi-normal-modes (QNMs) over a matching "comb" [27]. We use in general five QNMs; note, however, that for $\nu = 0$ three QNMs are sufficient to obtain good agreement between EOB and RWZ waveforms [29].

[4] Note that for the $\ell = m = 2$ mode the fit was done imposing the constraint that the 1PN coefficient is equal to 1, because $\rho^H_{22}(x;\,0) = 1 + x + \mathcal{O}(x^2)$.

III. TRANSMITTING LAYERS FOR THE REGGE-WHEELER-ZERILLI EQUATIONS

In this Section we describe the hyperboloidal layers adopted here to solve the RWZ equations and to extract the GW fluxes at the horizon and at null infinity. The method builds on previous work [30, 31, 38] and extends the hyperboloidal layer technique to the near-horizon regime. We also present, as a test of the implementation, the horizon absorbed fluxes from geodesic circular motion, and, in Appendix A, we report tail computations with our new infrastructure.

A. Smooth hyperboloidal layers

We use the Schwarzschild time coordinate t and the tortoise coordinate r_* in the bulk for describing the inspiralling particle using the standard EOB formalism. The tortoise coordinate

$$r_* = r + 2M \log(r - 2M), \tag{15}$$

is constructed such that the event horizon $r = 2M$ is at infinite coordinate distance. From a numerical point of view, the main effect of the tortoise coordinate is to push away the coordinate singularity at the bifurcation sphere in Schwarzschild coordinates. The computational domain is then truncated at some negative value for r_* and ingoing boundary conditions are applied.

There are two problems with this common approach. First, the artificial truncation of the computational domain leads to artificial boundary conditions. This problem is not as important in the negative r_* direction as in the positive one, because the potential falls off exponentially in the tortoise coordinate towards the horizon whereas only polynomially towards spatial infinity. Nevertheless, the imposition of such artificial boundary conditions can still complicate the implementation of higher order discretization methods. Second, the computation of absorbed fluxes by the black hole is performed at finite radius. To avoid contamination of the horizon flux computation by the artificial boundary conditions, a large grid in the negative r_* direction needs to be chosen (see, for example, [39]). This practice leads to a waste of computational resources.

A resolution to these problems is to change the coordinates near the horizon and in the asymptotic domain ("near infinity"), while keeping the standard Schwarzschild coordinates in the bulk. In our previous studies [29, 30] we applied hyperboloidal scri-fixing in a layer [31, 38] to solve these problems near infinity. In its original form, such a hyperboloidal layer is attached in the positive radial direction only so that the outer boundary corresponds to future null infinity. Since we are using the tortoise coordinate r_*, a similar layer can be attached also in the negative r_* direction so that the inner boundary corresponds to the black hole horizon. The time foliation in this layer is then not hyperboloidal but horizon penetrating. Nevertheless, we will keep using the term hyperboloidal layer for this new construction because the foliation has hyperboloidal properties in the tortoise coordinate.

The method consists of a spatial coordinate compactification and a time transformation as described below.

1. *Spatial compactification.*

Consider a finite domain $\mathcal{D}$ in the tortoise coordinate r_* given by $\mathcal{D} = [-R_-, R_+]$ where $R_\pm \in \mathbb{R}^+$. In this finite domain, we use coordinates (t, r_*). We introduce a compactifying coordinate[5] ρ to calculate the solution to the RWZ equations numerically on the unbounded domains $(-\infty, -R_-)$ and (R_+, ∞). The compactification is such that the infinities are mapped to a finite ρ, and at the interfaces $R_\pm$ the coordinates ρ and r_* agree.

A convenient way to write such a compactification is

$$r_* = \frac{\rho}{\Omega(\rho)}, \tag{16}$$

where $\Omega(\rho)$ is a suitable function of ρ. It is unity in the bulk domain, $\Omega_\mathcal{D} = 1$, implying $\rho = r_*$ on $\mathcal{D}$. For compactification, Ω must vanish at a finite ρ location, which then corresponds to infinity with respect to r_* (see [30, 31] for details). The transformation therefore is degenerate at the zero set of Ω. Its Jacobian reads

$$J \equiv \frac{d\rho}{dr_*} = \frac{\Omega^2}{\Omega - \rho\,\Omega'}, \tag{17}$$

where the prime indicates $d/d\rho$. A simple prescription for Ω to compactify both directions could be

$$\Omega = 1 - \left(\frac{|\rho| - R_\pm}{S_\pm - R_\pm}\right)^4 \Theta(|\rho| - R_\pm)\,, \tag{18}$$

For $\rho < 0$ we use the plus sign, for $\rho > 0$ we use the minus sign in the above formula. The transformation (16) with (18) maps the unbounded domain $-\infty < r_* < +\infty$ to the bounded domain $-S_- < \rho < S_+$ such that $\rho = r_*$ on $\mathcal{D} = [-R_-, R_+]$ where $S_\pm > R_\pm$.

The choice of Ω in (18) leads to a coordinate transformation that is C^4 at the interfaces. Our numerical experiments showed that this degree of smoothness was not sufficient for the accurate computation of late-time tail decay rates of the waveform reported in Appendix A. Numerical studies of hyperboloidal compactification using RWZ equations previously showed that a smooth (C^∞)

[5] For notational continuity with previous work we use the same symbol to address both the compactifying coordinate and the residual amplitude corrections $\rho_{\ell m}$ to the EOB waveform.

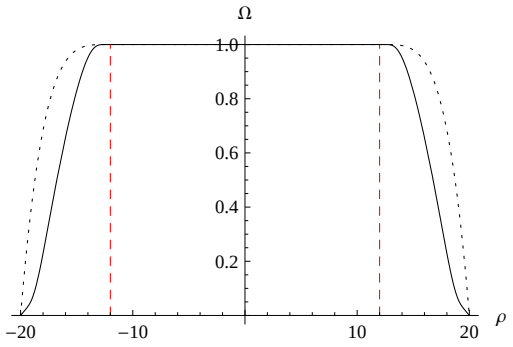

FIG. 1: The function Ω for the two choices (18) and (19). The dashed vertical lines (red online) indicate the interfaces at $R_\pm = 12$. Infinity corresponds to $S_\pm = 20$. The dashed (black online) curve denotes the C^4 transition (18), and the solid (black online) curve the smooth transition (19). The numerical results obtained later in the text are obtained with the smooth transition and with this choice of parameters.

transition leads to higher accuracy [40]. Such a smooth transition function can be given as

$$f_T := \frac{1}{2} + \frac{1}{2}\tanh\left[\frac{s}{\pi}\left(\tan x - \frac{q^2}{\tan x}\right)\right],$$

where we have defined

$$x := \left(\frac{\pi}{2}\frac{|\rho| - R_\pm}{S_\pm - R_\pm}\right).$$

The free parameter q determines the point $\rho_{1/2}$ at which $f_T(\rho_{1/2}) = 1/2$ and s determines the slope of f_T at $\rho_{1/2}$ [41, 42]. We set

$$\Omega = 1 - \frac{|\rho|}{S_\pm} f_T\,\Theta(|\rho| - R_\pm). \tag{19}$$

The two choices for Ω have been plotted in Fig. 1. For the main numerical results in this paper we use the smooth compactification of Eq. (19).

2. *Time transformation.*

It is well known that spatial compactification alone leads to resolution problems for hyperbolic equations [43]. The loss of resolution near infinity, however, can be avoided for essentially outgoing solutions by combining the spatial compactification with a suitable time transformation [31]. The details of this transformation depend on the background spacetime, but the essential idea is to keep the outgoing null direction invariant in local compactifying coordinates [30].

A suitable time transformation for numerical computations keeps the background metric invariant of the time coordinate by respecting the timelike Killing field [38]. Such time transformations can be written in the following form

$$\tau = t \pm h(r_*)\ , \tag{20}$$

where the function h is called the *height function* and depends on the tortoise coordinate only.

Near the black hole horizon, and near null infinity, gravitational waves propagate predominantly in one direction along null rays. Near the black hole most waves are absorbed, near infinity most waves escape. Correspondingly, near the black hole we require invariance of ingoing null rays in local coordinates, whereas near infinity we require invariance of outgoing null rays. The sign in Eq. (20) depends therefore on the sign of r_*. The invariance of the null direction in local compactifying coordinates translates into

$$t \pm r_* = \tau \pm \rho.$$

With Eq. (20) we get

$$r_* = \rho + h$$

or by defining $H := dh(r_*)/dr_*$

$$H = 1 - J. \tag{21}$$

This relation between the differential time transformation H and the differential spatial compactification J solves the resolution problem of compactification in hyperbolic equations.

We emphasize that, even though the inner hyperboloidal layer changes the time foliation, we do not modify the particle trajectory consistently when solving the RWZ equation. In principle, the particle motion should be expressed in the local coordinates of the inner layer. In practice, however, this seems unnecessary when the layer is attached at a sufficiently small negative value of $r_* = -R_- < 0$. We find that after the particle has crossed the light ring at $3M$, thereby triggering the QNM ringdown, its subsequent trajectory does not influence the waveform. Choosing $R_- = 12$ allows us to leave the description of the particle untouched. Once the particle enters the layer, we smoothly switch off the RWZ source to avoid unphysical features in the ringdown waveform (see Fig. 16 of [30]).

B. Horizon fluxes for circular orbits

As a test of the accuracy of our new numerical setup, and in particular, of the inner layer, we consider a point-particle moving on circular orbits of a Schwarzschild black hole and we compute the horizon fluxes. The treatment of the distributional δ-function describing the point-particle source as a finite-size, narrow Gaussian is the same as previous works [26–30]. Given a selected sample of stable and unstable orbits of radius r ($3.1 \leq r \leq 7.9$ spaced by $\Delta r = 0.1$), the RWZ waveform at the horizon location $\Psi^{(H,\epsilon)}_{\ell m}$, and its time derivative, $\dot\Psi^{(H,\epsilon)}_{\ell m}$, the fluxes of energy and angular momentum ab-

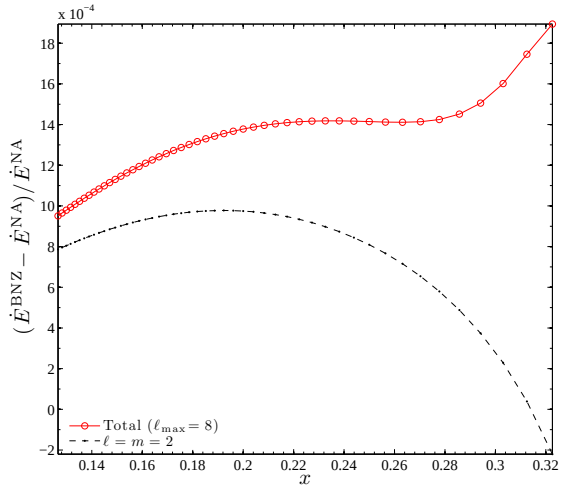

FIG. 2: (color online) Testing the accuracy of the updated time-domain RWZ code for a particle along a sequence of stable and unstable circular orbits. We plot the fractional difference in the horizon fluxes computed with the time-domain RWZ code using hyperboloidal layers and S. Akcay's frequency-domain code [3, 44].

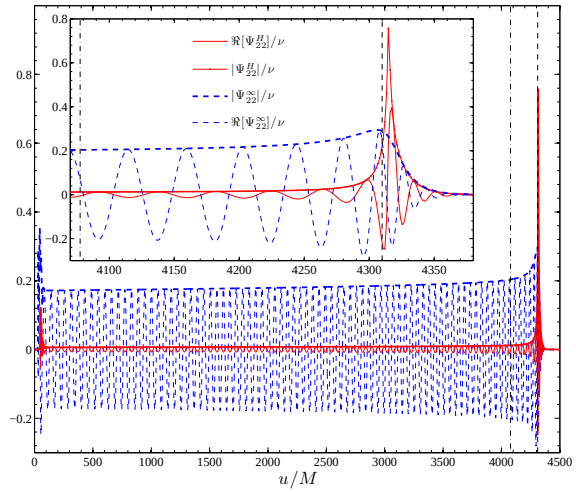

FIG. 3: (color online) Comparing horizon and null infinity quadrupolar ($\ell = m = 2$) RWZ waveforms for a coalescing binary with mass ratio $\nu = 10^{-3}$. The horizontal axis corresponds to horizon anticipated time $u \equiv u^+ = \tau + H$ for the horizon waveform and to null infinity retarded time, $u \equiv u^- = \tau - S$ for the asymptotic waveform. The leftmost (dash-dotted) vertical line marks the (dynamical) time when the particle crosses the LSO, while the rightmost (dashed) vertical line corresponds instead to the light-ring crossing. The horizon waveform (red online) becomes unreliable around the light-ring crossing ($u/M \gtrsim 4300$). See text for discussion.

sorbed by the black hole are given by [39]

$$\dot{E}^H_{(\ell_{\rm max})} = \frac{1}{16\pi}\sum_{\ell=2}^{\ell_{\rm max}}\sum_{m=0}^{\ell}\sum_{\epsilon=0}^{1}\frac{(\ell+2)!}{(\ell-2)!}|\dot{\Psi}^{(H,\epsilon)}_{\ell m}|^2 \tag{22}$$

$$\dot{J}^H_{(\ell_{\rm max})} = -\frac{1}{8\pi}\sum_{\ell=2}^{\ell_{\rm max}}\sum_{m=1}^{\ell}\sum_{\epsilon=0}^{1} m\frac{(\ell+2)!}{(\ell-2)!}\Im\left[\dot{\Psi}^{(H,\epsilon)}_{\ell m}\Psi^{(H,\epsilon)*}_{\ell m}\right] . \tag{23}$$

In Fig. 2 we show the fractional difference (plotted versus $x = 1/r = (M\Omega)^{2/3}$) between the the energy flux $\dot{E}^H$ computed with our code (labeled by "BNZ") and the same quantity obtained by S. Akcay using his frequency domain code [44], and presented for the first time in Ref. [3] (labeled by "NA"), i.e., $(\dot{E}^{\rm BNZ} - \dot{E}^{\rm NA})/\dot{E}^{\rm NA}$. The solid (red online) curve in the plot refers to the total flux summed up to $\ell_{\rm max} = 8$, while the dashed one to the $\ell = m = 2$ dominant quadrupole mode only. The frequency domain computation of horizon fluxes using the code of Ref. [44] have fractional uncertainty of order 10^{-10} or smaller for strong-field orbits (say $r \leq 10$). Figure 2 highlights how the fractional difference between the fluxes obtained with the two methods is on the order of 10^{-3}.

IV. HORIZON ABSORPTION IN THE LARGE-MASS-RATIO LIMIT

A. Perturbative, time-domain computation

In this section we compute the horizon-absorbed GW fluxes in a large-mass-ratio BBH coalescence using the perturbative method discussed extensively in previous works [26–30]. The computations allow us to test the reliability of the EOB-resummed fluxes given by Eq. (9).

In the large-mass-ratio limit the EOB Hamiltonian tends to the Schwarzschild one, and higher-order corrections in the analytical radiation reaction are neglected. The radiation-reaction term is then given by

$$\hat{\mathcal{F}}_\varphi \equiv \hat{\mathcal{F}}^{\mathscr{I}}_\varphi + \hat{\mathcal{F}}^H_\varphi = -\frac{32}{5}\nu r^4\Omega^5\left[\hat{f}^{\mathscr{I}}(v^2_\varphi;0) + \hat{f}^H(v^2_\varphi;0)\right], \tag{24}$$

with $v_\varphi = r\Omega$. Here, $\hat{f}^{\mathscr{I}}(v^2_\varphi;0)$ is computed as in Ref. [6] in the $\nu = 0$ limit but retaining all terms up to 5PN fractional accuracy in the $\rho_{\ell m}$'s computed in Ref. [45] (see also Ref. [46] for the 14PN accurate calculation).

We work here with the mass ratio [6] $\nu = 10^{-3}$. Previous

[6] Note that in the test-mass limit, $M_A/M_B \ll 1$ we can identify

studies [28, 30] indicated that, in this case, the method gives a fractional agreement between the 5PN-accurate mechanical angular momentum loss and the actual angular momentum flux computed from the RWZ master function of order 10^{-3} even beyond the LSO (see Fig. 14 of [30].) The RWZ master function is extracted numerically using the method of Sec. III. Neglecting horizon absorption in the dynamics ($\hat{f}^H(v_\varphi^2;0)=0$, in Eq. (24)), we reproduce the relative dynamics of previous works [28–30]. The initial relative separation is $r_0 = 7$ and the relative dynamics is started with the usual post-circular initial conditions [8, 26].

Figure 3 focuses on the $\ell = m = 2$ mode and illustrates the relative importance of the horizon waveform $\Psi^{(H,0)}_{22}$ compared to the asymptotic waveform $\Psi^{(\mathscr{I},0)}_{22}$. The figure shows on the same panel the real part of the waveforms together with their amplitudes. In the strong–field regime under consideration, $r \lesssim 7$, the horizon waveform is smaller (~ 16 times during inspiral) than the asymptotic waveform but not negligible (roughly comparable to some asymptotic subdominant multipoles). Notably, one finds that $|\Psi^{(H,0)}_{22}|$ is always *larger* than $|\Psi^{(\mathscr{I},0)}_{44}|$. The ratio between the two varies between 1.5 at the beginning of the inspiral up to 2 at LSO crossing.

The amplitude of the horizon waveform grows during the late plunge and reaches about 0.1 just before the light-ring crossing, $u/M \approx 4300$. It then increases by a factor ~ 7 over a temporal interval ~ 15, developing a "spike" that is twice as large as the corresponding value of the asymptotic amplitude. After this transient, the ringdown asymptotic and horizon waveforms are consistent.

The presence of a spike in the horizon waveform is due to our representation of the point-particle source as a narrow ($\sigma \ll 1$) Gaussian. The RWZ function is (in the $\sigma \to 0$ limit) discontinuous at $r_* = R(t)$ and its spatial derivative is singular. Since we have not implemented a sophisticated regularization of the source (see in this respect Refs. [47–50]), there is a spatial (smoothed) singularity on the RWZ computational grid at the particle location. After the particle has crossed the light ring, the singularity is advected to the horizon. The presence of such a discontinuity in the RWZ function and the corresponding singularity in the energy flux (also observed in the analytical treatment of an extreme-mass-ratio plunge by Hamerly and Chen [51]), makes our numerical representation of the particle ill-suited for a detailed study of horizon absorption during the last moments of the merger. We have, however, verified that the effect is localized around the location of the particle and its influence is reduced for smaller values of σ. In this work, we use the RWZ horizon waveform (and flux) only before the light-ring crossing, say $u/M \sim 4300$, so that our results

the inverse mass ratio $1/q = M_A/M_B$ with the *symmetric* mass ratio $\nu = M_A M_B/(M_A+M_B)^2$.

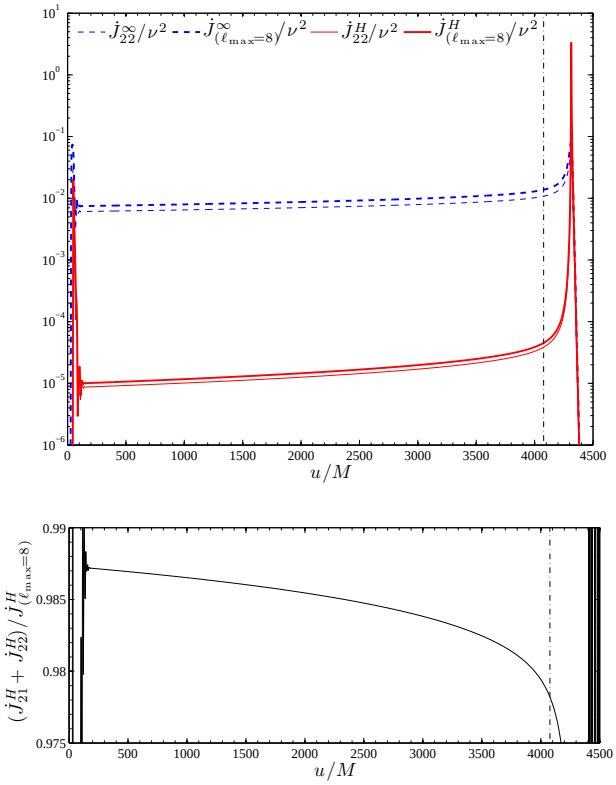

FIG. 4: (color online). Top panel: comparison between RWZ horizon and asymptotic angular momentum fluxes for mass ratio $\nu = 10^{-3}$ from Eq. (23) with $\ell_{\rm max} = 8$. Bottom panel: the $\ell = 2$ modes contribute to more than the 98% of the total absorbed flux up to LSO crossing (vertical dashed line).

are not affected by the absorption of the particle by the horizon.

We display in Fig. 4 the horizon-absorbed angular momentum flux $\dot{J}^H_{\ell_{\rm max}}/\nu^2$ computed from Eq. (23) with $\ell_{\rm max} = 8$. The top panel contrasts asymptotic fluxes (either summed up to $\ell_{\rm max} = 8$ or just $\ell = m = 2$), with the horizon fluxes, highlighting that the latter are typically 10^{-3} times smaller. The bottom panel of the figure shows the ratio between the total quadrupole horizon flux (i.e., $\dot{J}^H_{21} + \dot{J}^H_{22}$) and the total horizon flux $\dot{J}^H_{(\ell_{\rm max}=8)}$, which indicates that the quadrupole mode accounts for more than the 98% of the absorption up to the LSO crossing (dash-dotted vertical line in the plot).

B. The EOB-resummed horizon flux

We compare the horizon absorbed angular momentum flux computed from the RWZ waveform, Eq. (23), with the EOB-defined mechanical angular momentum loss due to horizon absorption, Eq. (24). In this section, the dynamics is computed including only $\hat{\mathcal{F}}^{\mathscr{I}}_\varphi$; the effect of $\mathcal{F}^H_\varphi$ is explored in the next section. Figure 5 shows the dom-

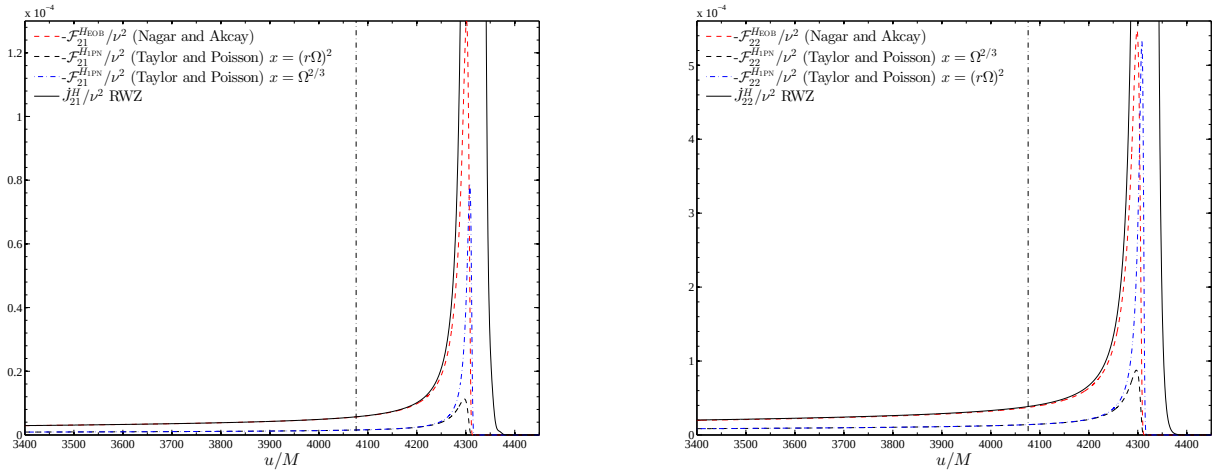

FIG. 5: (color online) Comparison between EOB resummed angular momentum flux and the RWZ one for the quadrupole ($\ell = 2$) modes: $m = 1$ (left panel) and $m = 2$ (right panel). The dash-dotted vertical line line marks the LSO crossing. The EOB-resummed (horizon) mechanical angular momentum loss shows very good consistency with the horizon flux computed from GWs. By contrast, the 1PN-accurate expressions, Eqs. (25)-(26), underestimate horizon absorption by more than a factor 2.

inant quadrupole $\ell = 2$ fluxes for $m = 1$ (left panel) and $m = 2$ (right panel). The mechanical losses $-\hat{\mathcal{F}}_{22}^{H}/\nu$ computed with various approximations (non-solid lines) are contrasted with $\dot{J}_{2m}^{H}/\nu^2$ (solid lines) The vertical dash-dotted line marks the LSO crossing. In addition to the EOB resummed analytical expressions (dashed curves, red online), we also show the PN-expanded (1PN-accurate) absorbed fluxes as computed by Taylor and Poisson [2], (see also Eq. (13) of [3]). They are given by

$$-\mathcal{F}_{22}^{H_{\rm 1PN}}(x) = \frac{32}{5}\nu^2 x^{15/2}(1+3x), \tag{25}$$

$$-\mathcal{F}_{21}^{H_{\rm 1PN}}(x) = \frac{32}{5}\nu^2 x^{17/2}. \tag{26}$$

When plotting these expressions we use two different PN representations of x: either $x \equiv v_\phi^2$ (dashed-line, black online) consistently with the EOB waveform, or $x_\Omega = \Omega^{2/3}$ (dash-dotted line, blue online). The two expressions differ only well below the LSO due to the violation of the Kepler constraint during the plunge.

Following observations can be made in Fig. 5. First, the PN expanded expressions clearly underestimate the absorbed flux in the strong-field regime. This is expected due to the structure of the $\rho_{\ell m}^{H}$ in the circular case. It has been shown in Ref. [3] (Fig. 3) that at $x = 1/7 \approx 0.14$ the 1PN-accurate ρ_{22}^{H} is more than a factor of two smaller than the corresponding $\rho_{22}^{H_{\rm num}}$ computed from numerical data.

Second, the EOB resummed expression (with the *fitted* coefficients $c_i^{\ell m}$) shows a very good consistency with the exact angular momentum flux computed from the waves. For the $\ell = m = 2$ mode, the fractional difference is $\approx 1\%$ at the beginning of the inspiral, to grow then up to $\approx 3\%$ at the LSO crossing. Notably, an excellent agreement occurs also for the $m = 1$ flux (fractional difference $< 1\%$ at LSO crossing), where the knowledge of the function ρ_{21}^{H} comes completely from the fit to the circular data [3]. The fractional difference we find here is approximately one order of magnitude larger than for the asymptotic flux (for the same mass ratio $\nu = 10^{-3}$), see Fig. 14 of [30]. This difference is not surprising because we have little analytical information to compute the EOB horizon flux. The computation relies mostly on the coefficients $c_i^{\ell m}$ obtained from the fit to the numerical data.

Third, the fluxes stay close also *below* the LSO crossing, even though we do not expect the RWZ fluxes to be accurate close to the light-ring crossing. The fact that the fluxes remain so close during the late inspiral up to the plunge is by itself a confirmation that the fitted c_i's yield a rather accurate approximation to the coefficients one would get from the analytic PN calculation.

In conclusion we have shown that the analytical expression of $\mathcal{F}_\varphi^H$, built using several pieces of information coming from a circularized binary (either analytical or numerical) shows an excellent agreement with the exact horizon flux computed from the RWZ waves. This makes us confident that we can safely use $\mathcal{F}_\varphi^H$ as a new term in the radiation reaction to take horizon absorption into account. The influence of this term on the waveform phasing will be discussed in detail below.

C. Effect on BBH phasing

In this section we discuss and quantify the effect of the inclusion of absorbed fluxes, $\mathcal{F}_\varphi^H$, in the dynamics on the observable GW (i.e. at infinity) from coalescing nonspinning binaries of different mass ratios. We work

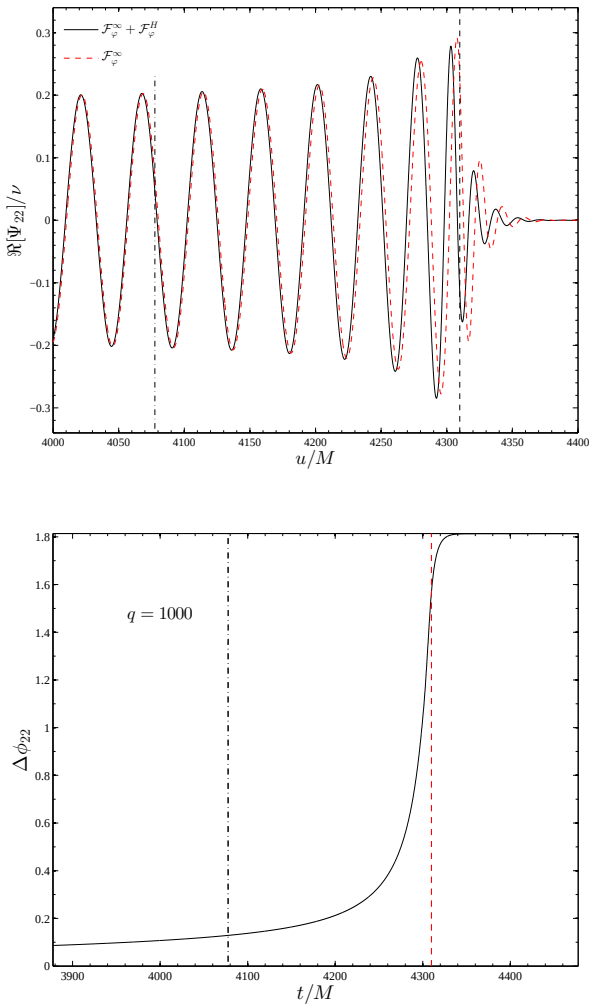

FIG. 6: (color online) Test-mass limit ($\nu = 10^{-3}$): including $\mathcal{F}_\varphi^H(v\,;0)$ in the dynamics and its effect on the $\ell = m = 2$ phasing. The top panel compares the $\ell = m = 2$ EOB waveforms with (solid line) and without (dashed line) $\mathcal{F}_\varphi^H(v;0)$. The accumulated phase difference (bottom panel) is of order 0.1 rad at LSO crossing (dash-dotted vertical line), and reaches a remarkable 1.5 rad at merger (dashed vertical line).

here only with EOB-generated waveforms.

We focus first on the test-mass limit, $\nu = 10^{-3}$, subject to leading-order (in ν) radiation reaction, Eq. (24) (we neglect then all the higher-order ν-dependent corrections). The effect of $\hat{f}^H(v_\varphi^2;0)$ on the $\ell = m = 2$ phasing is illustrated in Fig. 6. The initial separation is, as before, $r_0 = 7$, which yields about 41 orbits up to merger (see Table II). The top panel displays the EOB waveform without including horizon absorption (dashed line) together with the one where BH absorption is taken into account. The leftmost vertical line marks the LSO crossing, while the rightmost vertical line the light-ring crossing. The visible difference between the two waveforms is made quantitative in the bottom panel of the figure, where the phase difference is shown. Here it is $\Delta\phi_{22} = \phi^{H+\mathscr{I}} - \phi^{\mathscr{I}}$. One sees that the phase difference is 0.1 rad at the LSO and grows up to 1.6 rad at merger.

We turn now to compare a set of GWs from binaries with $q = 1, 4, 10, 50, 100$ and 1000, computed using the complete EOB dynamics. We run the simulations with and without horizon absorption and we compute the phase differences. The initial separation for $q = 1000$ is $r_0 = 7$, while for the other mass ratios it is $r_0 = 15$, corresponding to the initial GW frequency $M\omega_{22}^0 = 0.0344$. The result of this comparison is displayed in Fig. 7 and completed quantitatively by Table II. In the four panels of Fig. 7, the vertical lines mark, respectively from the left, the adiabatic LSO crossing and the EOB-defined light-ring crossing, i.e. the conventional location of the merger. First of all, we notice that even in the equal-mass case, where absorption effects are smallest and the system has a limited number of cycles, one gets a dephasing of the order of 5×10^{-3} rad at the EOB merger. Remarkably, this value is comparable to (or just a little bit smaller than) the uncertainty on the phase of the most accurate numerical simulations of (equal-mass, nonspinning) coalescing black-hole binaries currently available [36, 52, 53].

For higher mass ratios the cumulative effect of a larger horizon absorption (acting over more GW cycles) produces larger and nonnegligible dephasings. As listed in Table II, mass ratios of $q \sim 10$ to 100 accumulate (respectively) a dephasing of $\Delta\phi_{22}^{\rm LSO} \sim 0.06$ to 0.6 rad at LSO which increases by a factor of 3 near the light ring, $\Delta\phi_{22}^{\rm LR} \sim 0.22$ to 2.2 rad. The last two columns in Table II list the dephasings obtained using the non-resummed (1PN-accurate) radiation reaction. Interestingly, using such an expression of the absorbed flux yields dephasings that are up to 30% smaller ($q = 100$) at merger than the EOB prediction, underestimating the actual effect of absorption.

Since horizon absorption effects on phasing are relatively large, especially for $q > 50$, they may be relevant in template modeling for large-mass-ratio binaries. In particular, we focus on IMR binaries made by a stellar-mass compact object (SMCO) and an intermediate mass black-hole (IMBH), $(M_A, M_B) \sim (1, 50 - 500)M_\odot$, that are candidate sources for Advanced LIGO [21], and for the Einstein Telescope (ET) [22]. We perform an indicative calculation of the faithfulness $\mathcal{A}$ [54] of an EOB template without absorption effects in describing a waveform with absorption effects. Given two (real) waveforms, say h_1 (with horizon absorption) and h_2 (without horizon absorption) the *faithfulness* functional [54] (also denoted with the symbol $\mathcal{F}$ [55]) is defined as

$$\mathcal{A}[h_1, h_2] \equiv \max_{\alpha,\tau} \frac{(h_1, h_2)}{||h_1||||h_2||}, \tag{27}$$

where the maximization is performed over a relative time τ and phase shift α between the waveforms, and

$$(h_1, h_2) \equiv 4\Re \int_0^\infty df \frac{\tilde{h}_1(f)\tilde{h}_2^*(f)}{S_n(f)}, \tag{28}$$

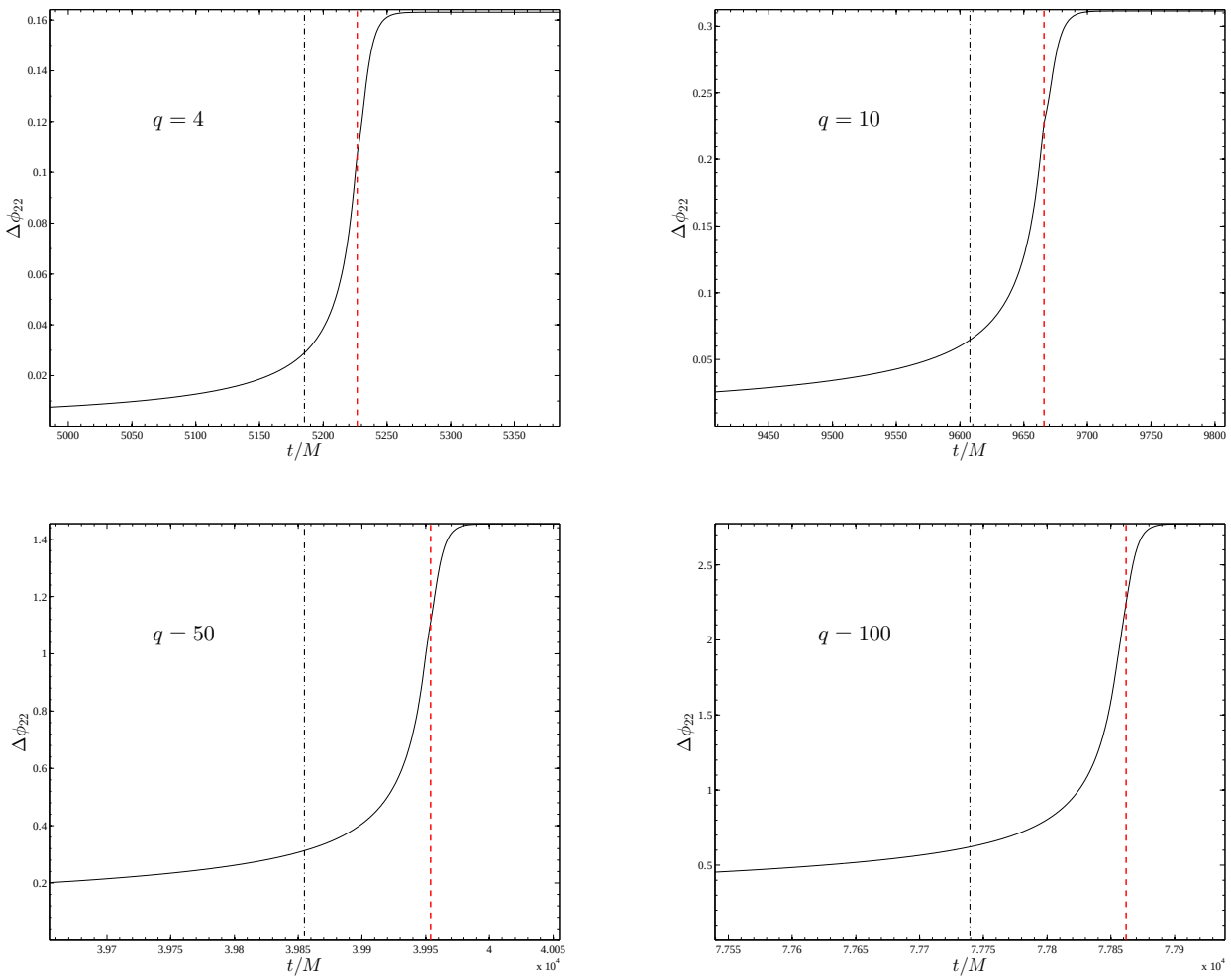

FIG. 7: (color online) Accumulated phase difference due to horizon absorption for different mass ratios q as obtained from EOB evolutions. The vertical lines mark the crossing of the EOB-defined LSO (leftmost line) and of the EOB-defined light-ring (rightmost line). For all binaries, the initial separation is $r_0 = 15$, corresponding to $M\omega_{22}^0 = 0.0344$.

defines the Wiener scalar product between the two signals. Here, $S_n(f)$ is the one-sided power spectral density of the detector noise, $\tilde{h}(f)$ the (complex) Fourier transform of the signal, and $||h|| = (h,h)^{1/2}$ the norm associated to the Wiener scalar product. The mass ratios considered were $q = 10$, 50, 71.4286 and 100, corresponding to total masses $M = (10+100)M_\odot$, $(10+500)M_\odot$, $(1.4+100)M_\odot$, and $M = (14+140)M_\odot$. We followed the technical steps of Ref. [55] to compute accurately the Fourier transform of an EOB waveform. We computed the faithfulness $\mathcal{A}$ taking for S_n both the `ZERO_DET_HIGH_P` anticipated sensitivity curve of Advanced LIGO [56] and that of the planned Einstein Telescope (ET) [57–59]. The numerical values of $\mathcal{A}$ are listed in Table III. Neglecting horizon absorption (for nonspinning binaries) leads to a loss of events ($\propto \mathcal{A}^3$) of, at most, 0.27% (for LIGO) and 0.9% for ET. These numbers can be considered negligible for practical purposes.

As a last remark, we argue that absorption fluxes in the nonspinning case are negligible also for parameter estimation. We computed a simplified *effectualness* functional [54] by considering a maximization over the total binary mass only. For the most relevant case $q = 100$, $M = 141.4M_\odot$ and the ET sensitivity curve, we found that $\max_M \mathcal{A} = 0.998$. A more detailed study of the effectualness would need maximization over every physical parameter of the system (e.g., the chirp mass, the symmetric mass ratio ν and the spins). Such an extended analysis should be performed for the spinning case, where horizon absorption effects are more relevant.

V. CONCLUSIONS

We investigated the importance of horizon absorption effects in modelling GWs from nonspinning coalescing

TABLE II: Accumulated phase differences due to to horizon absorption for different mass ratios. The data of the first six binaries are obtained from a complete EOB simulations. On the contrary, the dynamics of the last binary, shown for comparison, is that of a point-particle driven by leading-order radiation reaction only. For the first five binaries, the initial separation is $r_0 = 15$, which corresponds to frequency $M\omega_0^{22} \approx 0.0344$, while the last two binaries start at $r_0 = 7$, i.e. $M\omega_0^{22} = 0.108$. From left to right, the columns report: the mass ratio q; the symmetric mass ratio $\nu = q/(1+q)^2$ ($\nu = 1/q$ for the last binary); the initial separation; the number of orbits up to merger (EOB-defined light-ring crossing), $N_{\rm orb}$; the dephasing $\Delta\phi_{22} = \phi_{22}^{H+\mathscr{I}} - \phi_{22}^{\mathscr{I}}$ accumulated at the (adiabatic) EOB-defined LSO crossing; the corresponding value expressed in GW cycles; the dephasing accumulated at the EOB-defined light-ring crossing; the corresponding value expressed in GW cycles. The rightmost two columns show the phase difference accumulated using Taylor-Poisson, nonresummed, 1PN accurate radiation reaction. Note that the effect of horizon absorption on the phasing is still nonegligible (for $q \geq 10$) even using this leading order approximation to $\hat{\mathcal{F}}_\varphi^H$.

q	ν	r_0	$N_{\rm orb}$	$\Delta\phi_{22}^{\rm LSO}$ [rad]	$\Delta\mathcal{N}^{\rm LSO}$	$\Delta\phi_{22}^{\rm LR}$ [rad]	$\Delta\mathcal{N}^{\rm LR}$	$\Delta^{\rm 1PN}\phi_{22}^{\rm LSO}$ [rad]	$\Delta^{\rm 1PN}\phi_{22}^{\rm LR}$ [rad]
1	0.250000	15	15	0.003289	0.000523	0.005475	0.000871	0.002849	0.004547
4	0.160000	15	21	0.028725	0.004572	0.104712	0.016665	0.012320	0.020246
10	0.082645	15	38	0.064372	0.010245	0.220496	0.035093	0.052834	0.199428
50	0.019223	15	153	0.312210	0.049690	1.115319	0.177508	0.230220	0.765105
100	0.009803	15	296	0.620662	0.098781	2.217042	0.352853	0.458168	1.549226
1000	0.000998	7	41.2	0.129978	0.020687	1.453992	0.231410	...	...
1002	0.000996	7	40.9	0.129023	0.020535	1.563971	0.248914	...	...

TABLE III: Faithfulness between signals with and without horizon flux for SMCO-IMBH (nonspinning) binaries in the Advanced LIGO and Einstein Telescope sensitivity band. The merger frequency $f_{\rm merger}$ corresponds to the maximum of the EOB waveform modulus $|h_{22}|$

q	$M_A + M_B [M_\odot]$	$f_{\rm merger}$ [Hz]	$\mathcal{A}_{\rm aLIGO}$	$\mathcal{A}_{\rm ET}$
10	$10 + 100$	89.16	0.9999	0.9998
50	$10 + 500$	17.92	0.9991	0.9995
71.43	$1.4 + 100$	89.21	0.9991	0.9983
100	$1.4 + 140$	63.63	0.9992	0.9970

black hole binaries. Considering a recently proposed EOB resummed expression of the absorbed flux [3], we verified the EOB expression against perturbative waveforms from large mass ratio ($q = 1000$) binaries (Sec. IV), and explored the effects of absorbed fluxes on the phasing considering EOB evolutions for binaries of different mass ratios $q = 1$ to 1000 (Sec. IV C).

We tested the accuracy of the analytically resummed horizon flux [3], and in particular of the residual amplitude corrections $\rho_{\ell m}^H$, in the large-mass-ratio, perturbative limit. We compared it to the actual horizon flux of angular momentum computed solving the Regge-Wheeler-Zerilli equations in the time-domain.

To improve the accuracy of the perturbative computation, we employed two hyperboloidal layers [31] (horizon-penetrating near the horizon and hyperboloidalnear null infinity) attached to a compact domain in standard Schwarzschild coordinates. This technique, summarized in Sec III, allows us to include in the computational domain both null-infinity, $\mathscr{I}$, and the horizon, H, via compactification in the tortoise coordinate. The resulting improvements of our perturbative time-domain code combined with high-order finite differencing lead to such accurate computations of the inspiral and plunge that the late-time tail of the signal can be calculated very efficiently as reported in Appendix A.

We computed the absorbed GW fluxes from the transition from inspiral to plunge down to the late inspiral up to merger for the first time. We found that the quadrupolar contributions dominate over the subdominant multipoles accouting for about 98% of the absorbed radiation (see bottom panel of Fig. 4). The $\ell = 2$ absorbed angular momentum flux from the perturbative simulations proved to be consistent at the 1% level with the analytical expressions proposed in [3]. Notably, the agreement remains excellent also below the LSO crossing and during the plunge. The resummation procedure for the flux introduced in [3] and the numerical determination of the higher-order PN terms entering the $\rho_{\ell m}^H$ amplitude corrections were crucial to obtain this result. The 1PN accurate, Taylor-expanded expression of the horizon flux as computed by Taylor and Poisson [2], underestimates horizon absorption by as much as a factor 2 during the late-inspiral and plunge phases.

The absorbed flux of [3] has been used to build an additional term to the radiation reaction force of the EOB model, $\mathcal{F}_\varphi^H$, thereby incorporating in the model, in a resummed way, horizon absorption. By means of EOB simulations we explored its effect on the phasing of the GW emitted by binaries of different mass ratios q. Even in the current nonspinning case, it yields nonnegligible phase differences for $q > 1$. In particular, in the

mass-ratio range $q = 10$ to 100 (see Table II), the accumulated phase differences are of the order 0.2 to 2 rad up to merger for circularized binaries initially at relative separation of $r_0 = 15$. By contrast, the PN-expanded radiation reaction underestimates the dephasing by 9% to 48% (depending on q).

Finally, we have performed a preliminary investigation of the impact of horizon absorption on the accurate modeling of templates for IMR nonspinning binaries made by a SMCO and a IMBH $(M_A, M_B) \sim (1, 50-500)M_\odot$. We found that neglecting $\mathcal{F}^H_\varphi$ would yield a loss of events by 0.27% for Advanced LIGO and by 0.9% for ET. These losses are essentially negligible by current accuracy standards.

Horizon absorption effects are more important for spinning binaries. It will be necessary to include them in $\mathcal{F}^H_\varphi$, after a suitable resummation procedure, so to study their impact on the phasing. Similarly, we expect their influence to be nonnegligible on faithfulness and effectualness computations for gravitational wave data analysis purposes.

Acknowledgments

We are grateful to S. Akcay for the numerical data of Fig. 2, and D. Pollney for giving us access to the NR data of [35, 37]. We thank T. Damour for useful suggestions, and N.K. Johnson-McDaniel for reading the manuscript. SB is supported by DFG GrantSFB/Transregio 7 "Gravitational Wave Astronomy." S. B. thanks IHES for hospitality and support during the development of part of this work. A. Z. is supported by the NSF Grant No. PHY-1068881, and by a Sherman Fairchild Foundation grant to Caltech. Computations were performed on the `MERLIN` cluster at IHES.

Appendix A: Late-time tail decay for radial infall and insplunge trajectories

In this Appendix we present, for the first time, the accurate computation of the late-time power-law tail of the waveform at $\mathscr{I}$, generated by a particle plunging, both radially and following an inspiralling trajectory, into a Schwarzschild black hole. This result completes the knowledge of the $\mathscr{I}$-waveform for these events, already computed elsewhere [29, 30].

We recall that the gravitational waveform is computed by solving the RWZ equations in the time domain for each multipole. The δ-function representing the particle is approximated by a narrow Gaussian of finite width $\sigma \ll M$, Eq. (A1). The representation of a particle as a Gaussian is a standard method when gravitational perturbations are computed using finite-difference, time-domain methods. This representation, however, was considered problematic, because time-domain codes gave relatively inaccurate results for gravitational fluxes [60–62]. Therefore, different prescriptions have been experimented with to improve on the representation of the point particle through a Gaussian [63–65]. Nevertheless, the accuracy of time domain codes remained low, especially when compared with frequency domain ones. One open problem was the calculation of tail decay rates for a particle radially infalling into a Schwarzschild black hole [61].

Recently, a multi-domain hybrid method of finite difference and spectral discretizations has been developed to solve this problem [66]. With this method, and using a large computational domain, the polynomially decaying part of the signal could be computed. However, the width of the Gaussian used in [66] to represent the particle is inadequate for the particle limit. In fact, the "particle" in this study is larger than the Schwarzschild black hole that provides the background.

In this Appendix, we show that the accuracy provided by hyperboloidal layers, combined with high-order finite differencing, allows us to calculate the tail decay rates accurately for realistic representations of a point particle in Schwarzschild spacetime. We present the decay rates not only for a radially infalling particle, but also for an insplunging one.

As in previous work [26, 28–30], we approximate the delta distribution that represents the particle at time-dependent location, $R_*(t)$, by a Gaussian

$$\delta(r_* - R_*(t)) \;\to\; \frac{1}{\sqrt{2\pi}\sigma} \exp\left(-\frac{(r_* - R_*(t)^2}{2\sigma^2}\right). \quad \text{(A1)}$$

Our prescription for the standard deviation, σ, depends on resolution. We set $\sigma = 4\,\triangle r_*$, so that the Gaussian is resolved well on our finite difference grid.

Transmitting layers play an essential role in resolving narrow Gaussians because they allow us to compute the infinite domain solution in a small grid. This implies that the numerical resolution is not wasted in simulating empty space; instead, it can be focussed to where the particle is located. As a consequence, we can afford to choose $\triangle r_*$, and therefore the width of the Gaussian σ, very small.

Another advantage of using the layer method is that the implementation of high-order finite differencing becomes simpler because there are no boundary conditions to be applied at either end of the domain. Note that even when good boundary conditions are available, their discretization and numerical implementation may not be straightforward. When no boundary conditions need to be applied, however, using a high order finite difference method becomes just a matter of widening the stencils.

Using hyperboloidal layers, we have improved the accuracy of our previous work [30]. We use a smaller domain of $[-20, 20]$ with interfaces at $R_\pm = \pm 12$. Compared to our previous domain of $[-50, 70]$, this gives us a factor of

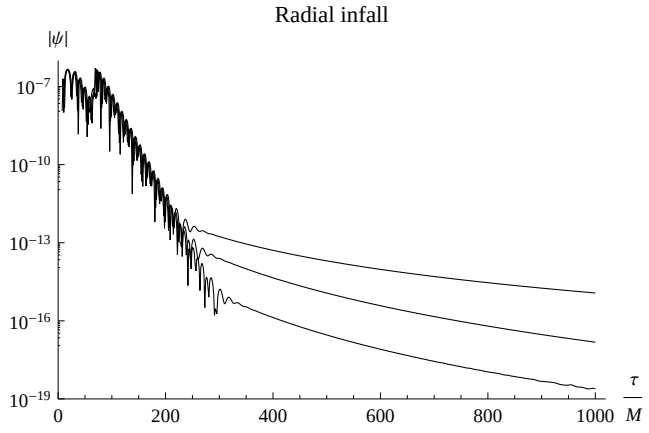

FIG. 8: The evolution of the field for a radially infalling particle starting at $r_0 = 7$. The plot spans 13 orders of magnitude. Observers are located (from top to bottom) at $\mathscr{I}$, 30, and 15.

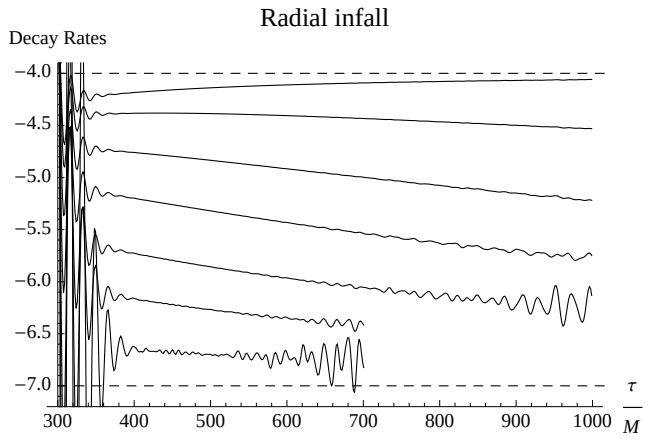

FIG. 9: The local decay rates for the above evolution. The observers are located approximately at (from top to bottom) in units of M: $\{\mathscr{I}, 250, 80, 50, 35, 25, 20\}$. The dashed lines indicate the theoretically expected asymptotic decay rates: -4 at $\mathscr{I}$, and -7 at finite distances.

3 in efficiency [7]. In addition, we use 8th order finite differencing as opposed to 4th order in [30]. As a result, we can compute the tail decay rates accurately, as reported below.

1. Radial infall

The calculation of gravitational perturbations caused by a particle falling radially into a non-rotating black hole is a classical problem in relativity [67, 68]. It serves as a good test bed for numerical computations, and there are still relatively recent studies on the problem [61, 66, 69].

We solve the radial infall of a particle to demonstrate the accuracy of our infrastructure. For a detailed description of the setup, the reader is referred to the literature [39, 47, 48, 70].

In Fig. 8, we show the absolute value of the Zerilli function ψ_{20} caused by an infalling particle initially at rest at $r_0 = 0$ as measured by three observers. The particle is represented by the Gaussian (A1) with a full width at half maximum (FWHM)[8] of $0.04M$. We use 10,000 grid cells and a time stepping factor of 0.75 for the computation. Note that, differently from Refs. [47, 48] we put $\psi_{20} = 0$ initially and we do not solve consistently the Hamiltonian constraint. Since we are interested here in the late-time behavior of the waveform, this simplifying choice has no influence on our results. We see the QNM ringing after the plunge of the particle into the black hole, followed by late-time decay. The three curves in the figure correspond to the measurements of three observers (from top to bottom): the observer at infinity, the finite distance observer at $30M$, and at $15M$. The perturbations are computed for about $1000M$ which leads to a drop in the absolute value of the perturbation by 13 orders of magnitude. The polynomially decaying signal is reproduced accurately.

The gain in accuracy is partly a result of the 8th order finite differencing, but mostly due to the high resolution we can afford using hyperboloidal layers, which allow us not only to compute the perturbations as measured by the observer at infinity, but also to follow the signal much longer than is possible with standard methods. For example, in Ref. [66] the authors compute the perturbations until about $600M$ for a Gaussian source that has a FWHM of $5 - 10M$ which is larger than the size of the central black hole, and therefore cannot represent a realistic particle[9].

We also plot the local decay rates as measured by different far away observers in Fig. 9. The local decay rate plot gives a clear image of the accuracy of our computation. We see that the expected decay rates are reproduced accurately. The observer at infinity measures a rate of -4, whereas the rate for finite distance observers approaches -7. The intermediate behavior for the decay rates for these observers is in accordance with computations of vacuum perturbations [40].

The local rates for the observers at $25M$ and $20M$ in Fig. 9 have been cut from the plot at late times because of large oscillations. The loss of accuracy for these observers is not only because of accumulated truncation error, but mostly because the fast decaying signal reaches machine

[7] By construction, reducing domain size does not decrease the time step for a given resolution. We did not attempt to find the optimal thickness for the layers.

[8] The FWHM of a normal distribution is given by its standard deviation σ as $2\sigma\sqrt{2\ln 2}$.

[9] The representation of the Gaussian in [66] leads to a FWHM of $2\sqrt{\sigma \ln 2}$. The authors present studies with σ ranging between 10 and 50.

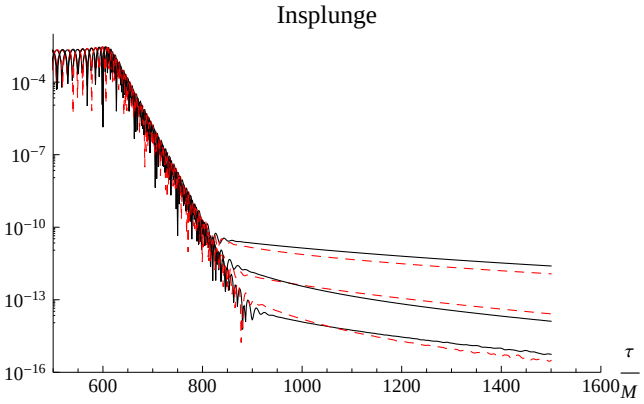

FIG. 10: The evolution of the real (solid line) and imaginary (dashed line) of the field for insplunge from $r_0 = 7$. The evolution spans 14 orders of magnitude. Observers are located (in units of M, from top to bottom) at $\mathscr{I}$, 35, and 18.

precision. If necessary, the decay rate calculation can be further improved by using quadruple precision, and possibly higher resolution.

2. Insplunge

The main interest in this paper is the study of particles plunging into the central black hole following a phase of quasi-circular inspiral (insplunge). We compute the tail decay rates also for this case. As above, the initial separation is $r_0 = 7$. In Fig. 10 we show the absolute value of the real part (solid line) and imaginary part (dashed line) of the perturbation, again as measured by three observers (from top to bottom): the observer at infinity and the finite distance observers at $35M$ and $18M$. The computational parameters are the same as in the radial infall study. We see that the field is followed for 14 orders of magnitude, and the evolution is presented until $1500M$ this time. The three stages of the evolution (inspiral, ringing, and polynomial decay) are clearly visible. The local decay rates show qualitatively the same behavior as in Fig. 9 and are therefore not plotted.

[1] K. Alvi, Phys.Rev. **D64**, 104020 (2001), gr-qc/0107080.
[2] S. Taylor and E. Poisson, Phys.Rev. **D78**, 084016 (2008), 0806.3052.
[3] A. Nagar and S. Akcay, Phys.Rev. **D85**, 044025 (2012), 1112.2840.
[4] R. H. Price and J. T. Whelan, Phys.Rev.Lett. **87**, 231101 (2001), gr-qc/0107029.
[5] G. Lovelace, M. Boyle, M. A. Scheel, and B. Szilagyi, Class.Quant.Grav. **29**, 045003 (2012), 17 pages, 7 figures, submitted to Classical and Quantum Gravity, 1110.2229.
[6] T. Damour, B. R. Iyer, and A. Nagar, Phys. Rev. **D79**, 064004 (2009), 0811.2069.
[7] A. Buonanno and T. Damour, Phys. Rev. **D59**, 084006 (1999), gr-qc/9811091.
[8] A. Buonanno and T. Damour, Phys. Rev. **D62**, 064015 (2000), gr-qc/0001013.
[9] T. Damour, Phys. Rev. **D64**, 124013 (2001), gr-qc/0103018.
[10] E. Poisson and M. Sasaki, Phys.Rev. **D51**, 5753 (1995), gr-qc/9412027.
[11] E. Barausse and A. Buonanno, Phys.Rev. **D81**, 084024 (2010), 0912.3517.
[12] E. Barausse and A. Buonanno, Phys.Rev. **D84**, 104027 (2011), 15 pages, 7 figures. Reference added, typos fixed. Matches version accepted for publication in PRD, 1107.2904.
[13] A. Nagar, Phys.Rev. **D84**, 084028 (2011), 1106.4349.
[14] A. Taracchini, Y. Pan, A. Buonanno, E. Barausse, M. Boyle, et al. (2012), 1202.0790.
[15] N. Yunes, A. Buonanno, S. A. Hughes, Y. Pan, E. Barausse, et al., Phys.Rev. **D83**, 044044 (2011), 1009.6013.
[16] N. Yunes, A. Buonanno, S. A. Hughes, M. Coleman Miller, and Y. Pan, Phys. Rev. Lett. **104**, 091102 (2010), 0909.4263.
[17] A. Taracchini, A. Buonanno, S. A. Hughes, and G. Khanna (2012), in preparation.
[18] J. A. Gonzalez, U. Sperhake, and B. Bruegmann, Phys.Rev. **D79**, 124006 (2009), 0811.3952.
[19] C. O. Lousto and Y. Zlochower, Phys.Rev.Lett. **106**, 041101 (2011), 1009.0292.
[20] U. Sperhake, V. Cardoso, C. D. Ott, E. Schnetter, and H. Witek, Phys.Rev. **D84**, 084038 (2011), 1105.5391.
[21] D. A. Brown, H. Fang, J. R. Gair, C. Li, G. Lovelace, et al., Phys.Rev.Lett. **99**, 201102 (2007), accepted for publication in Physical Review Letters, gr-qc/0612060.
[22] E. Huerta and J. R. Gair, Phys.Rev. **D83**, 044021 (2011), 1011.0421.
[23] E. Huerta and J. R. Gair, Phys.Rev. **D84**, 064023 (2011), 1105.3567.
[24] E. Huerta, J. R. Gair, and D. A. Brown, Phys.Rev. **D85**, 064023 (2012), 1111.3243.
[25] E. Huerta, P. Kumar, and D. A. Brown (2012), 1205.5562.
[26] A. Nagar, T. Damour, and A. Tartaglia, Class. Quant. Grav. **24**, S109 (2007), gr-qc/0612096.
[27] T. Damour and A. Nagar, Phys. Rev. **D76**, 064028 (2007), 0705.2519.
[28] S. Bernuzzi and A. Nagar, Phys. Rev. **D81**, 084056 (2010), 1003.0597.
[29] S. Bernuzzi, A. Nagar, and A. Zenginoglu, Phys.Rev. **D83**, 064010 (2011), 1012.2456.
[30] S. Bernuzzi, A. Nagar, and A. Zenginoglu, Phys.Rev. **D84**, 084026 (2011), 1107.5402.
[31] A. Zenginoglu, J.Comput.Phys. **230**, 2286 (2011), 1008.3809.
[32] T. Damour and A. Nagar, Phys. Rev. **D79**, 081503 (2009), 0902.0136.
[33] Y. Pan, A. Buonanno, M. Boyle, L. T. Buchman, L. E. Kidder, et al. (2011), 1106.1021.
[34] T. Damour and A. Gopakumar, Phys. Rev. **D73**, 124006 (2006), gr-qc/0602117.
[35] S. Bernuzzi, T. Damour, A. Nagar, D. Pollney, C. Reiss-

wig, and Z. Anil, In preparation (2012).
[36] D. Pollney, C. Reisswig, E. Schnetter, N. Dorband, and P. Diener, Phys.Rev. **D83**, 044045 (2011), 0910.3803.
[37] T. Damour, A. Nagar, D. Pollney, and C. Reisswig, Phys.Rev.Lett. **108**, 131101 (2012), 1110.2938.
[38] A. Zenginoglu, Class. Quant. Grav. **25**, 145002 (2008), 0712.4333.
[39] K. Martel, Phys.Rev. **D69**, 044025 (2004), gr-qc/0311017.
[40] A. Zenginoglu, Class. Quant. Grav. **27**, 045015 (2010), 0911.2450.
[41] N. Yunes, W. Tichy, B. J. Owen, and B. Bruegmann, Phys.Rev. **D74**, 104011 (2006), gr-qc/0503011.
[42] I. Vega, P. Diener, W. Tichy, and S. L. Detweiler, Phys.Rev. **D80**, 084021 (2009), 0908.2138.
[43] C. E. Grosch and S. A. Orszag, J. Comput. Phys. **25**, 273 (1977).
[44] S. Akcay, Phys. Rev. **D83**, 124026 (2011), 1012.5860.
[45] R. Fujita and B. R. Iyer, Phys. Rev. **D82**, 044051 (2010), 1005.2266.
[46] R. Fujita (2011), 1104.5615.
[47] C. O. Lousto and R. H. Price, Phys.Rev. **D55**, 2124 (1997), gr-qc/9609012.
[48] K. Martel and E. Poisson, Phys.Rev. **D66**, 084001 (2002), gr-qc/0107104.
[49] L. Barack, Class.Quant.Grav. **26**, 213001 (2009), 0908.1664.
[50] E. Poisson, A. Pound, and I. Vega, Living Rev.Rel. **14**, 7 (2011), 1102.0529.
[51] R. Hamerly and Y. Chen, Phys.Rev. **D84**, 124015 (2011), 1007.5387.
[52] M. A. Scheel et al., Phys. Rev. **D79**, 024003 (2009), 0810.1767.
[53] C. Reisswig, N. Bishop, D. Pollney, and B. Szilagyi, Phys.Rev.Lett. **103**, 221101 (2009), 0907.2637.
[54] T. Damour, B. R. Iyer, and B. Sathyaprakash, Phys.Rev. **D57**, 885 (1998), gr-qc/9708034.
[55] T. Damour, A. Nagar, and M. Trias, Phys.Rev. **D83**, 024006 (2011), 1009.5998.
[56] D. Shoemaker (2010), https://dcc.ligo.org/cgi-bin/DocDB/ShowDocument?docid=2974.
[57] A. Freise, S. Chelkowski, S. Hild, W. Del Pozzo, A. Perreca, et al., Class.Quant.Grav. **26**, 085012 (2009), 0804.1036.
[58] M. Punturo, M. Abernathy, F. Acernese, B. Allen, N. Andersson, et al., Class.Quant.Grav. **27**, 194002 (2010).
[59] B. Sathyaprakash, M. Abernathy, F. Acernese, P. Ajith, B. Allen, et al., Class.Quant.Grav. **29**, 124013 (2012), 1206.0331.
[60] L. M. Burko and G. Khanna, Europhys.Lett. **78**, 60005 (2007), gr-qc/0609002.
[61] J.-H. Jung, G. Khanna, and I. Nagle, Int.J.Mod.Phys. **C20**, 1827 (2009), 0711.2545.
[62] J. L. Barton, D. J. Lazar, D. J. Kennefick, G. Khanna, and L. M. Burko, Phys.Rev. **D78**, 064042 (2008), 0804.1075.
[63] P. A. Sundararajan, G. Khanna, and S. A. Hughes, Phys.Rev. **D76**, 104005 (2007), gr-qc/0703028.
[64] P. A. Sundararajan, G. Khanna, S. A. Hughes, and S. Drasco, Phys.Rev. **D78**, 024022 (2008), 0803.0317.
[65] P. A. Sundararajan, G. Khanna, and S. A. Hughes, Phys.Rev. **D81**, 104009 (2010), 1003.0485.
[66] D. Chakraborty, J.-H. Jung, and G. Khanna, Int.J.Mod.Phys. **C22**, 517 (2011), 1103.1551.
[67] F. Zerilli, Phys.Rev. **D2**, 2141 (1970).
[68] M. Davis, R. Ruffini, W. Press, and R. Price, Phys.Rev.Lett. **27**, 1466 (1971).
[69] E. Mitsou, Phys.Rev. **D83**, 044039 (2011), 1012.2028.
[70] A. Nagar and L. Rezzolla, Class.Quant.Grav. **22**, R167 (2005), gr-qc/0502064.